nature energy

Article

https://doi.org/10.1038/s41560-026-01967-1

Mechanistic understanding of interphase-driven ageing in silicon anodes

Received: 24 April 2024

Accepted: 31 December 2025

Published online: 03 February 2026

Check for updates

Weiran Zhang[1,2,7], Nan Zhang[2,7], Zeyi Wang[2,7], Ai-Min Li[2,7], Sufu Liu[2], Taeyong Lee[2], Yawei Chen[2], Yijie Liu[2], Zheng Li[2], Hongli Wan[2], Sz-Chian Liou[3], Jiancun Rao[3], Joseph Roschella[2], Lei Zheng[2], Zhiyuan Zhang[4], Huixin He[4], Brett L. Lucht[5], Christopher S. Johnson[6] & Chunsheng Wang[1,2]

Conventional solid electrolyte interphases (SEIs) strongly adhere to micro-silicon (μ-Si) and crack under volume changes, causing poor cycling performance. Nano-silicon improves cycling performance but remains costly with limited calendar life. Here potentiostatic ageing tests demonstrate that both calendar and cycle ageing are governed by SEI cracking and dissolution with different relative contributions. When the system is not dominated by SEI dissolution, the relative calendar life of Si anodes could correlates positively with their cycle life. LiF-rich SEI that enables long cycle life in μ-Si is therefore expected to enhance calendar life as well. Using this framework, we screened electrolytes, SEIs and electrodes and validated them with full-cell storage. LiF-rich SEI minimizes cracking and dissolution, enabling μ-Si to achieve excellent calendar life, whereas nano-silicon suffers from SEI dissolution and needs reduced electrolyte–electrode contact for better calendar life. This work clarifies calendar-ageing behaviour and accelerates electrolytes and SEI development for long-life Si anodes.

Lithium metal batteries offer high energy density[1,2] but face safety concerns and cost challenges due to high reactivity and limited resources[3,4]. Silicon (Si), with a high theoretical specific capacity of 3,579 mAh g^{-1}, is a safer, far cheaper and more abundant alternative, making it a strong candidate for <US$100 kWh^{-1} pack-level cost target[5,6]. However, high capacity of Si induces a significant volume change (~300%), causing cracking of both μ-Si particles and organic-rich SEIs formed in commercial carbonate electrolytes[7,8]. The resulting in electrolyte penetration and continual SEI reformation induced active-material loss[9], electrode swelling, electrolyte and Li^+ consumption, thus poor cycling coulombic efficiency (cCE) and cycle life. Reducing the particle size to nano-Si (n-Si), including nanowires[10,11], nano-film[12], core-shell nanostructures[10], hollow particles[13] and porous Si[14], could suppress the cracking and improve cCE and cycle life[15]. However, the large surface area of n-Si causes substantial Li^+ consumption, decreasing the initial CE[16,17], limiting the practical application of full cells[18–20]. Although pre-lithiation of n-Si can partially offset Li^+ consumption, the challenges of high cost and shortened calendar life remain[16,17,21,22].

Due to lack of understanding on calendar ageing, many factors, including active-material loss, gas evolution, SEI breathing, binder reaction and HF etching, have been suggested to the short calendar life of Si anodes[16,17,23–25]. Advanced architecture designs improved cycle life of Si-containing cells, the calendar life (~2 years) remains far shorter than that of graphite[26] and well below the target of 10 years[16], hindering the commercial development of Si anodes.

In this work, we investigated the calendar-ageing mechanism of Si electrodes by varying the SEI composition and Si particle size. We adopted the Department of Energy's (DOE) silicon consortium project

[1]Department of Materials Science and Engineering, University of Maryland, College Park, MD, USA. [2]Department of Chemical and Biomolecular Engineering, University of Maryland, College Park, MD, USA. [3]Institute for Research in Electronics and Applied Physics, University of Maryland, College Park, MD, USA. [4]Department of Chemistry, Rutgers, the State University of New Jersey, Newark, NJ, USA. [5]Department of Chemistry, University of Rhode Island, Kingston, RI, USA. [6]Chemical Sciences and Engineering Division, Argonne National Laboratory, Lemont, IL, USA. [7]These authors contributed equally: Weiran Zhang, Nan Zhang, Zeyi Wang, Ai-Min Li. e-mail: cswang@umd.edu

voltage-hold calendar life testing protocol[27–29] to evaluate the Si anode calendar ageing mechanism, which is strongly related to SEI chemistry and surface area. The findings were supported by structural and chemical characterizations and validated through open-circuit voltage (OCV) full-cell ageing tests and USABC-style storage evaluations[30]. These results indicate that the calendar life of Si electrodes is primarily limited by SEI instability (cracking and dissolution), driving both active-materials loss and SEI repair/growth. This degradation mechanism is similar to that governing cycle life, but with different relative contributions from cracking and dissolution. When the SEI dissolution is not dominated, the relative calendar life of Si anodes could correlate positively with their cCE. LiF SEI on μ-Si anodes effectively suppresses cracking[31] and exhibits lower solubility[21,32],which show potential to achieve a calendar life comparable to that of graphite. On the other hand, the n-Si electrode suffers severe SEI dissolution due to its large surface area, limiting its calendar life. Recognizing the time-consuming nature of the calendar life test, this mechanistic framework linking calendar life to SEI composition, electrode particle size and cCE is important in preliminary screening towards long calendar life.

Calendar ageing mechanism of Si anodes

Both cycle and calendar life degradation originate from active-material loss and SEI growth caused by SEI instability (cracking and dissolution). As depicted in Fig. 1a, μ-Si volume changes cracks both particles and SEI. Cracking exposes fresh Si, triggering new SEI formation, isolating cracked Si (active-material loss) and accelerating SEI growth. In parallel, SEI continuously dissolve into the electrolytes[24,25,32], especially for organic compounds[21,33–35], driving SEI growth.

Although cycle life and calendar life share the exact fundamental mechanism, their emphasis differs. This emphasis also varies across different electrodes (Fig. 1b). During cycle-life tests, electrodes experience a full volume change over relatively short periods, during which SEI dissolution is limited. Thus, cycle life or cCE is dominated by cracking-induced active-material loss and cracking-induced SEI growth, with minimal contribution from SEI dissolution (Fig. 1b). Conversely, calendar life involves long-term storage, during which SEI dissolution becomes more significant than SEI cracking of volume change. However, silicon anodes still have slow yet detrimental volume changes during self-discharge[16], much larger than those of graphite, which is crack-free and thus serves as the benchmark in this work. Because calendar ageing does not involve the full volumetric changes encountered during electrochemical cycling, SEI cracking contributes less to calendar ageing than to cycle ageing. Nevertheless, both the SEI dissolution (governed by surface area and SEI solubility) and SEI cracking (governed by volume change and SEI stability) are critical to calendar ageing in Si anodes. This suggests calendar ageing could potentially correlate with cCE and SEI dissolution, with the SEI dissolution being strongly dependent on particle size. This dual dependence explains why calendar life does not always correlate directly with electrolytes' cCE, as seen in lithium metal systems[36] whose morphology (surface area) varies across electrolytes.

This framework explains many reported results. Because cycle and calendar life share the same mechanisms, certain systems may exhibit excellent performance in both cycle life and calendar life[16,17]. μ-graphite anode with organic–inorganic SEIs, which are flexible to accomodate 12% volume change without cracking (Fig. 1b), enable a high cCE of 99.98% with >1,000 cycle life. Moreover, the relatively small SEI surface area minimizes dissolution, enabling a 15-year calendar life[37]. Si-phobic LiF SEI on μ-Si significantly reduced the stress/strain of SEI due to weak bonding between LiF and Si. Therefore, SEI cracking is largely reduced, achieving a cCE of 99.9% with >400 cycle life[31,38]. Furthermore, LiF SEI has a low solubility and a high electron-blocking ability[39,40], thereby reducing Li^+ consumption for SEI growth (Fig. 1c, right). Therefore, LiF SEI is promising to help the development of Si calendar life comparable to that of μ-graphite electrodes (Fig. 1b).

On the other hand, because SEI cracking and dissolution have different relative contributions to calendar and cycle life, strategies that enhance cycle life may not necessarily enhance calendar life. n-Si effectively reduces SEI cracking, improving cycle life (Fig. 1b). However, n-Si also exhibits more pronounced SEI dissolution due to its large surface area, so the calendar life of n-Si-containing electrodes is far below μ-graphite[16,17,41–44] (Fig. 1c, left), when no strategies are applied to limit the electrode–electrolyte contact surface area.

Validation of the proposed calendar life mechanism

SEI instability is closely linked to SEI composition and associated properties: LiF-rich SEI suppresses cracking and dissolution, whereas organic-rich SEI is prone to both. It is also influenced by SEI surface area (particle size) and electrolyte amount. Commercial μ-graphite anodes, with minimal volume changes, primarily experience calendar ageing due to SEI dissolution. Thus, the graphite with carbonate electrolytes serve as a benchmark and performance target in our study.

The impact of SEI composition on μ-Si calendar life is investigated with four representative electrolytes: Li-anode-favoured high-concentration electrolytes (4 M LiFSI DME) and localized high-concentration electrolytes (1 M LiFSI DME/TTE)[45–47], μ-Si-favoured electrolytes (2 M $LiPF_6$ THF/MTHF)[31] and n-Si-favoured electrolytes (1 M $LiPF_6$ EC/DEC/FEC). These produced SEIs ranging from LiF-rich to organic rich (Supplementary Table 1), exhibiting notable difference in cycling performance (Supplementary Fig. 1): 2 M $LiPF_6$ THF/MTHF exhibits exceptional stability with μ-Si, whereas high-concentration and localized high-concentration electrolytes failed to effectively support μ-Si and carbonate electrolytes worked for n-Si but not μ-Si.

To fairly compare electrolytes, a fully formed SEI is required before the calendar test. Whereas most reports use three formation cycles for the graphite[27,48] and n-Si calendar life test[49], μ-Si requires more cycles due to its significant volume changes and cracking. On the basis of the number of cycles each electrolyte needs to reach its maximum cCE (Supplementary Fig. 1), we performed at least 15 formation cycles (Fig. 2a) and Si remain its original particle size after these formation cycles (Supplementary Fig. 2 and Supplementary Note 1).

The calendar ageing was evaluated using a modified voltage-hold protocol from DOE-silicon consortium[27–29], which expedites ageing by maintaining a constant voltage and offers higher time resolution than OCV storage protocols, allowing rapid observation of degradation trends[28]. Several key considerations are necessary for successfully implementing voltage-hold protocols, including careful selection of the counter electrode, maintaining sufficient lithium inventory with minimal potential variation and determining the appropriate hold duration and potential[29]. Here lithium metal was used as the counter electrode to provide an infinite lithium reservoir and a fully flat voltage profile (Supplementary Figs. 3 and 4 and Supplementary Note 2). This set-up ensures accurate state-of-charge control during the voltage hold and avoids repeated lithiation/delithiation caused by potential fluctuations, thereby minimizing the contribution of reversible relaxation processes in leakage current. In addition, it mitigates possible SEI crossover effects[50–52] and potential SEI oxidation[25] because Li and Si share similar SEI chemistry and potential (Supplementary Fig. 3). These make the Li||Si configuration a cleaner system in which observed calendar-life degradation can be attributed primarily to the Si anode.

Because reversible diffusion-relaxation processes can still occur during the initial voltage hold, an inverse polarization experiment (Supplementary Fig. 5) was used to determine the duration required for stabilization before assessing degradation[29] (Supplementary Note 3). The hold potential determines silicon utilization with corresponding reactivity[53] and kinetics[54]. Here we selected 60 mV for the Si anode, corresponding to high practical utilization while lying on a steeper voltage slope, which favours kinetics while suppressing reversible relaxation during voltage hold.

https://doi.org/10.1038/s41560-026-01967-1

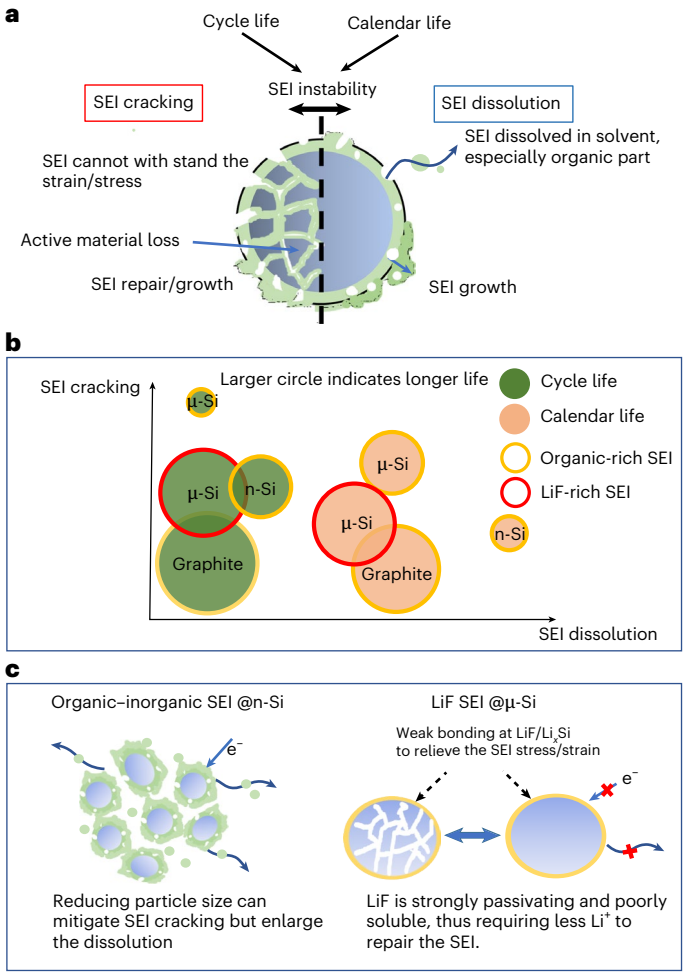

Fig. 1 | Schematic of calendar life in Silicon anode. a, Calendar life and cycle life are both determined by SEI instability (SEI cracking and SEI dissolution). **b**, The relative roles of SEI cracking and SEI dissolution in determining the cycle life and calendar life vary across different electrodes (n-Si, μ-Si, μ-graphite) and different SEI compositions (organic-rich, inorganic LiF-rich). Estimated data and properties from refs. 16,32,38,41–44. **c**, Difference between n-Si in organic SEI and μ-Si in LiF SEI. Reducing the particle size to nano-size can reduce the SEI cracking to improve the cycle life, but it will enlarge the SEI dissolution, thereby significantly decreasing the calendar life. By contrast, the LiF SEI has weak bonding to Li_xSi to relieve the stress/strain of SEI and suppress the SEI cracking so that the μ-Si without a large surface area can be used. Moreover, LiF has less solubility with a high passivation ability to reduce the Li^+ consumption in the calendar ageing.

Accordingly, Si anodes were cycled first and then potentiostatically held at 0.06 V, followed by references cycles (Fig. 2a). Their capacity plots are shown in Supplementary Fig. 6. The leakage current during voltage hold is monitored for 180 h (Fig. 2b). The initial rapid current drop arises from concentration overpotential, whereas the subsequent current leakage mainly captures dynamic response of SEI repair/growth resulting from SEI cracking and dissolution. Integrating of the leakage current yields the calendar ageing capacity loss Q_L (Supplementary Fig. 7), including both irreversible capacity loss and reversible relaxation.

To separately assess the active-materials loss, SEI repair/growth and irreversible capacity loss, we define four calendar ageing test metrics based on the DOE-silicon consortium protocol (Fig. 2c): (1) irreversible cycling Coulombic efficiency (1 − cCE), a capacity loss that assesses active-materials loss and SEI repair/growth due to SEI cracking (equation (1)), representing cycle instability. (2) Irreversible calendar Coulombic efficiency (1 − caCE) that access relative calendar ageing capacity loss from both active-materials loss and SEI growth (equation (2)), representing calendar ageing. (3) Active capacity loss that quantifies active-materials loss (equation (3)). (4) Leakage current@180 h of voltage hold that indicates SEI repair/growth rate. Detailed description is shown in Supplementary Note 4.

$$\text{Irreversible cycling Coulombic efficiency } (\%) = 1 - \text{cCE} \quad (1)$$

$$1 - \text{caCE} = (Q_D + Q_L - Q_C)/(Q_D + Q_L) = 1 - \frac{Q_C}{Q_D + Q_L} \quad (2)$$

$$\text{Active capacity loss } (\%) = 1 - Q_{D1}/Q_D \quad (3)$$

Both 1 − caCE and 1 − cCE reflect active-materials loss (SEI cracking) and SEI repair/growth (SEI cracking and SEI dissolution), whereas 1 − cCE effectively weights SEI dissolution by a factor X, where X increase with time and SEI surface area. X is negligible for micro-sized electrodes during short cycling tests. Thus cCE can partially predict the relative calendar life when dissolution is not dominated in calendar ageing (1 − caCE), as confirmed in Fig. 2d and Supplementary Fig. 8a. We extracted cCE values of μ-Si anodes at a standard 0.1 C after 15 cycles (Supplementary Fig. 1) in 2 M $LiPF_6$ THF/MTHF, 1 M LiFSI DME/TTE, 1 M $LiPF_6$ EC/DEC/FEC and 4 M LiFSI DME and obtained the 1 − cCE values as 0.3%, 0.8%, 1.6% and 4.9%. Systems with lower 1 − cCE also exhibit lower 1 − caCE, demonstrating a positive correlation between cycle and calendar ageing.

However, this correlation holds only for electrodes with similar particle sizes, as varying SEI surface areas alter dissolution contributions in calendar ageing. Thus, electrodes with different SEI surface areas may show little correlation between cCE and calendar life. This explains previous Li-metal studies[36] where calendar ageing was observed generally in both high- and low-cCE electrolytes: different electrolytes produce different lithium morphologies with different surface areas, breaking the correlation. Therefore, our observation here offers an early-stage screening metric.

This positive correlation compliments the conventional leakage-current method. Leakage current captures the overall SEI growth and is therefore highly reliable when active-material loss is minimal, such as in crack-free graphite, crack-less n-Si and μ-Si with LiF SEI. Moreover, it enables direct comparison across different electrode systems (for example, between graphite and Si). However, leakage current does not account for active-material loss, its predictive accuracy decreases when severe SEI cracking occurs. By contrast, cCE is applicable for system where SEI cracking is significant but is not suitable for comparing different electrode systems with varying surface areas. Therefore, a comprehensive prediction should consider both cCE and leakage current together.

The active-materials loss across different systems was measured using active capacity loss (%) (Fig. 2e and Supplementary Fig. 8b) and 'active capacity loss excluding cyclic decay' (Supplementary Fig. 9). As expected, the active-material loss increases with the decrease of inorganic content in SEI, because the organic-rich SEI is more prone to cracking under substantial volume change.

On the basis of the calendar-ageing metrics above, 1 − caCE captures both SEI growth and active-materials loss during calendar ageing. Therefore, if we assume calendar ageing is predominantly determined by the SEI cracking and dissolution, the capacity loss due to SEI growth (Fig. 2f) can be estimated by the difference between 1 − caCE and active-materials loss during calendar ageing. The leakage current @180 h, which represents the SEI growth rate, correlates closely with estimated SEI-growth capacity loss across electrolytes, supports this proposed framework. It is essential to acknowledge the contribution from other factors, such as binder reaction or gas evolution, but they are not limiting factors.

https://doi.org/10.1038/s41560-026-01967-1

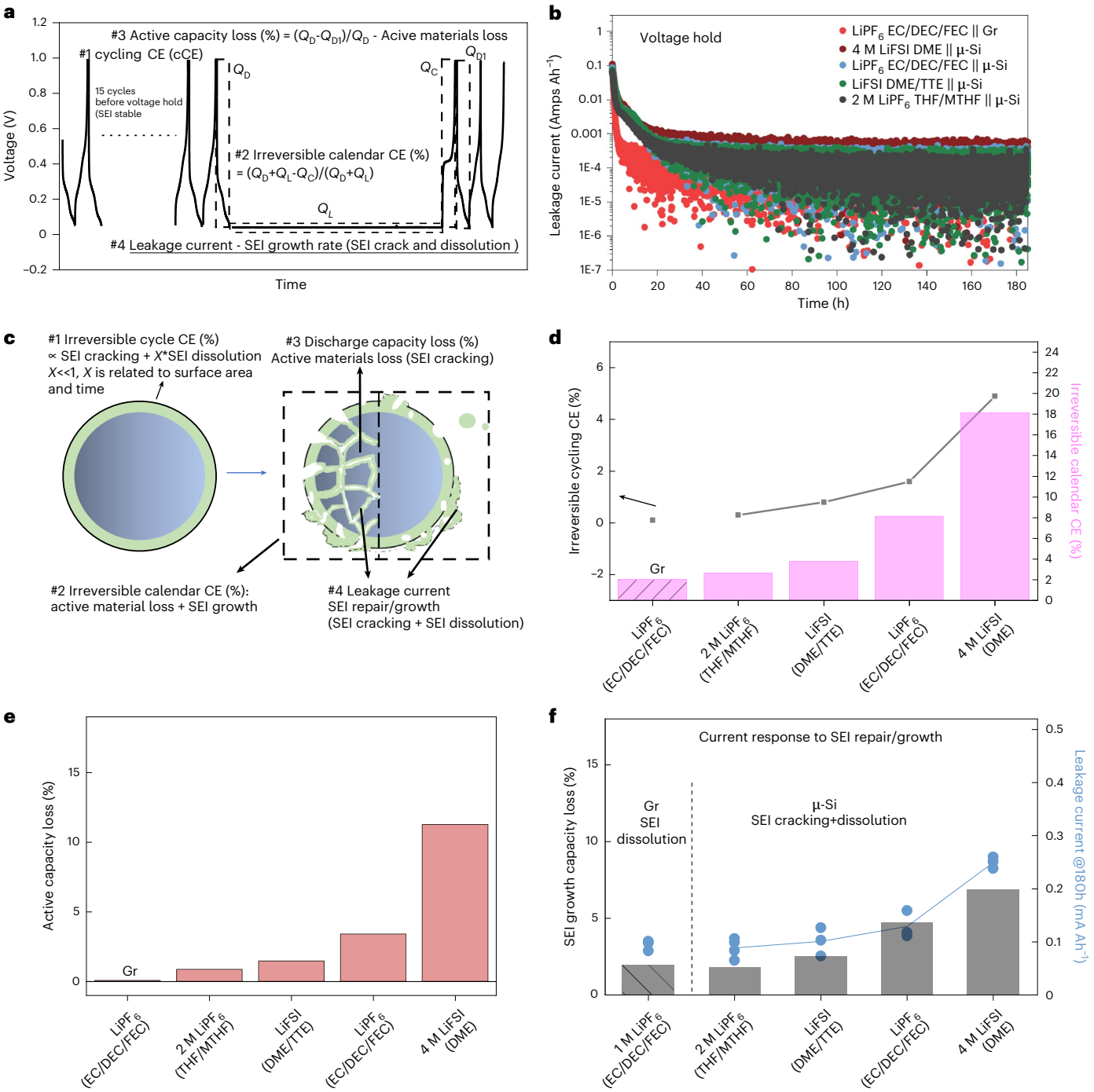

Fig. 2 | Calendar life of Si anodes with different electrolytes. a, Calendar life test protocols. As shown in the figure, Q_D is the discharge capacity before voltage hold, Q_C is the charge capacity after voltage hold, Q_L is the leakage capacity during voltage hold, Q_{D1} is the discharge capacity of the reference cycle after voltage hold. **b**, Leakage current collected in the Li | |μ-Si cell using different electrolytes, including ether (4 M LiFSI DME, 1 M LiFSI DME/TTE, 2 M $LiPF_6$ THF/MTHF) and carbonate-based electrolytes (1 M $LiPF_6$ EC/DEC/FEC). **c**, The metrics and mechanism to evaluate the calendar ageing. **d**, The irreversible calendar CE and irreversible cCE in a variety of systems, which are derived from reversible calendar CE and cycling CE in Supplementary Fig. 8a. **e**, The active capacity loss in a variety of systems, which is derived from discharge capacity retention in Supplementary Fig. 8b. **f**, The leakage current@180 h and estimated SEI growth capacity loss of Li | |μ-Si and Li | |graphite cells in a variety of electrolytes. Each point represents an independent sample.

SEI cracking

SEI cracking leads to active-materials loss and SEI growth. By comparing the 1 − caCE (Fig. 2d) of μ-Si and μ-graphite with the same 1 M $LiPF_6$ EC/DEC/FEC electrolytes, we can analyse the role of SEI cracking as their SEI dissolution are expected to be comparable. The μ-Si anode shows a higher leakage current than graphite (Fig. 2f), indicating greater SEI-crack-induced SEI growth. Whereas this significant SEI growth in Si anodes is commonly attributed to the higher reactivity and breathing of Si anode[16,55], our analysis identifies cracking-induced SEI growth as the primary contributor.

Across all electrolytes, μ-Si exhibits noticeable active capacity loss (Fig. 2e) in calendar ageing, driven by unavoidable SEI cracking during its large volume expansion. This active-materials loss is particularly problematic when the SEI is organic-rich. By contrast, the crack-free

https://doi.org/10.1038/s41560-026-01967-1

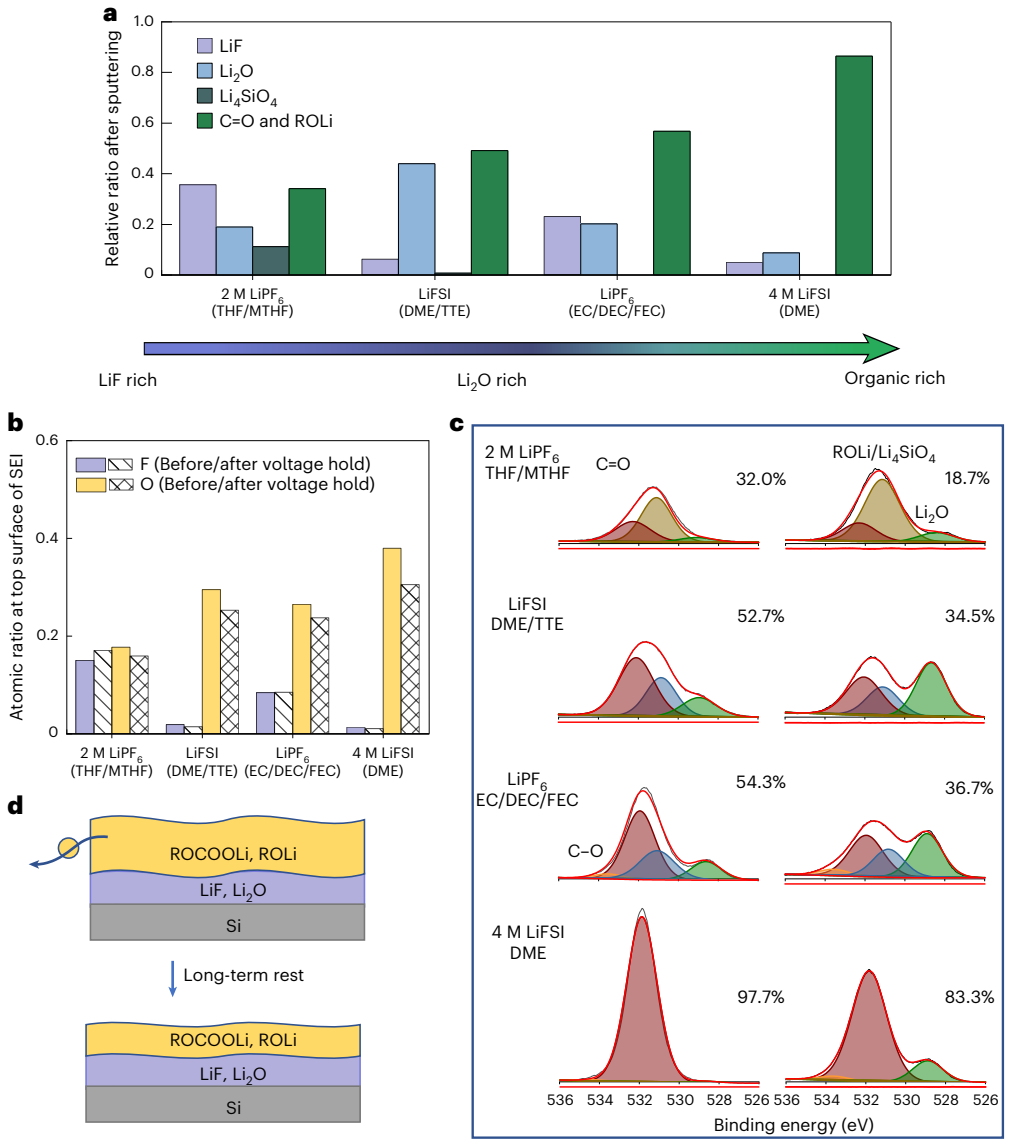

Fig. 3 | The SEI compositions in a variety of electrolytes and the passivation ability of these compositions. a, The relative ratio of LiF, Li_2O, Li_4SiO_4 and C=O with ROLi in SEI (after sputtering) of μ-Si anode cycled in 2 M $LiPF_6$ THF/MTHF, 1 M LiFSI DME/TTE, 1 M $LiPF_6$ EC/DEC/FEC, 4 M LiFSI DME before voltage hold. **b**, Fluorine and oxygen content ratio changes in the SEI (surface part) of four electrolytes before and after long-term voltage hold. **c**, XPS O spectra of upper SEI on μ-Si anode with four electrolytes before and after voltage hold, the ratio represents the C=O content ratio in O-based components. **d**, A schematic of the SEI dissolution during long-term storage.

graphite anode shows minimal active capacity loss and lowest irreversible calendar CE, highlighting that active-material loss induced by SEI cracking, often overlooked, is also a key contributor to μ-Si calendar ageing. 2 M $LiPF_6$ THF/MTHF can improve μ-Si calendar life, due to suppressed active-materials loss and SEI growth (Fig. 2e,f). Therefore, a silicon-phobic SEI is necessary to stabilize SEI for better calendar life.

Effect of SEI composition on SEI dissolution

When SEI cracking is limited, SEI dissolution becomes a dominant factor to consider during calendar ageing. SEI dissolution depends on the solubility of SEI composition, which is investigated by X-ray photoelectron spectroscopy (XPS) with an Ar^+ sputtering depth profiling (Supplementary Figs. 10 and 11), revealing mixture of inorganic (LiF, Li_2O and Li_4SiO_4) and organic (C=O, ROLi) components. The SEI compositions of four electrolytes systems follow a tendency from LiF-rich, Li_2O-rich, inorganic/organic, to organic-rich SEI (Fig. 3a and Supplementary Note 5), correlating with observed difference in cycling performance and calendar ageing.

To investigate SEI dissolution, we studied their composition before and after voltage hold. A clear difference in SEI composition after long-term voltage hold is observed (Fig. 3b). The F-content (mainly LiF) remains largely unchanged, whereas the O-content decreased significantly. Compositional analysis of O-based species on the surface of SEI (Fig. 3c and Supplementary Fig. 12) revealed that the loss was primarily due to organic components (C=O, ROLi). By contrast, LiF peak exhibited minimal changes, consistent with reports that LiF could be relatively permanent SEI composition[21,32,35]. After voltage hold, the C=O ratio significantly decreases in all four electrolytes, whereas Li_2O increases. This indicates that organic compositions (Li alkoxides, Li alkyl carbonates and so on) exhibit serious dissolution during the voltage hold while inorganic compositions are relatively insoluble (Fig. 3d). Higher electrolyte amounts also exacerbate SEI dissolution: tests with varying glass fibre layers (different electrolyte amounts) indicate that higher electrolyte amounts lead to higher leakage current (Supplementary Fig. 13), highlighting the need to control electrolyte amount for long calendar life.

https://doi.org/10.1038/s41560-026-01967-1

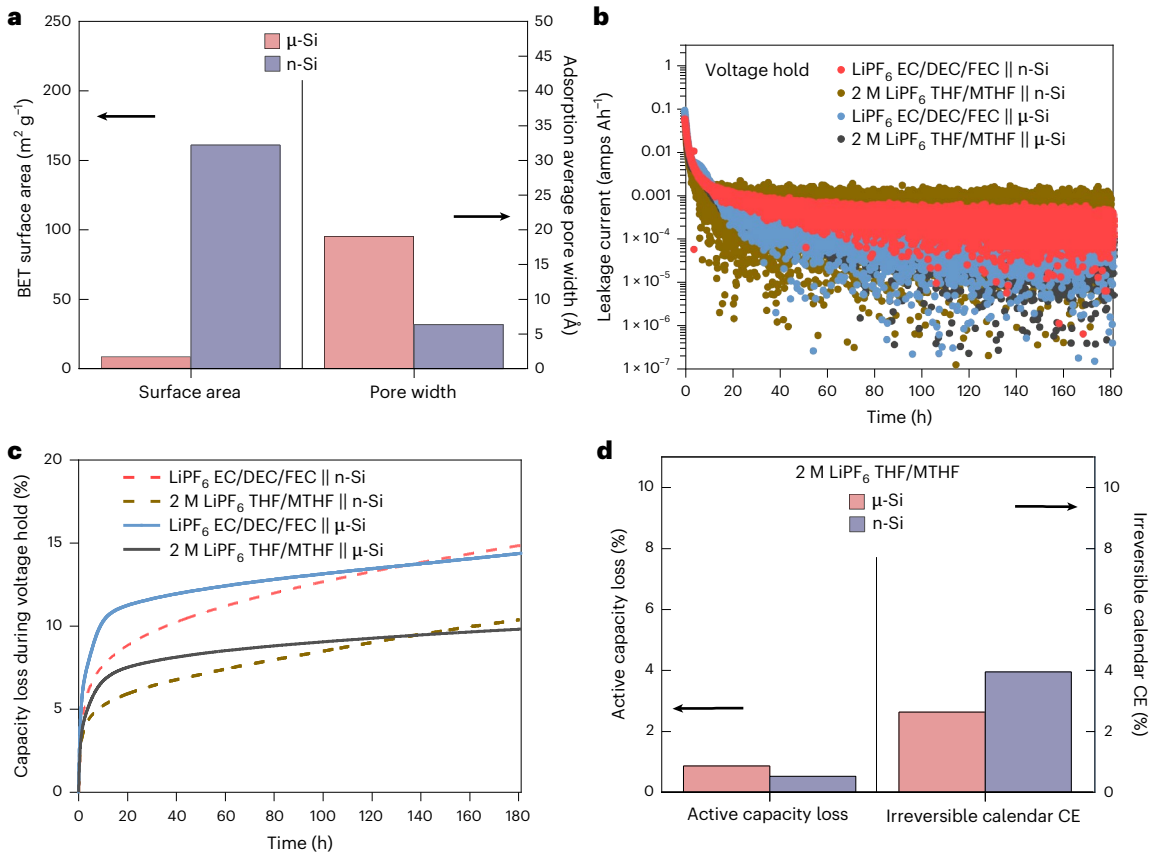

Fig. 4 | The calendar life of μ-Si vs n-Si. a, The BET surface area and adsorption average pore width of μ-Si and n-Si anode. **b**, Leakage current of the cell using μ-Si and n-Si electrodes, with 2 M $LiPF_6$ THF/MTHF and 1 M $LiPF_6$ EC/DEC/FEC electrolytes. **c**, The corresponding capacity leakage during voltage hold. **d**, Active capacity loss and irreversible calendar CE of μ-Si vs n-Si anode after calendar ageing, which is derived from the reversible calendar CE and discharge capacity efficiency in Supplementary Fig. 19.

Effect of surface area on SEI dissolution

Besides SEI composition, particle size significantly influences SEI dissolution by impacting the surface area. n-Si mitigates the stress on SEI and cracking but increases the surface area, making SEI dissolution the dominant mechanism in calendar ageing of n-Si. Here μ-Si and n-Si electrodes were fabricated with the same process and composition ratio, but n-Si exhibits a Brunauer–Emmett–Teller (BET) surface area of 161.033 $m^2 g^{-1}$, 19 times higher than μ-Si (Fig. 4a and Supplementary Fig. 14). n-Si also has much higher cumulative pore volume than μ-Si (Supplementary Fig. 15), though with smaller average pore width (Fig. 4a).

We selected 2 M $LiPF_6$ THF/MTHF (LiF SEI, good for μ-Si) and $LiPF_6$ EC/DEC/FEC (organic–inorganic SEI, good for n-Si) to investigate the impact of particle size on SEI dissolution, with same potentiostatic voltage to ensure comparable silicon utilization[53] (Supplementary Fig.16). As shown in Supplementary Figs. 1a,c and 17, n-Si anode suppresses cracking and exhibits notably improved cycling stability, but its larger surface area significantly increases the leakage current and capacity loss rate (Fig. 4b,c), for both LiF-rich SEI and organic–inorganic SEI. As a result, although the active-materials loss of n-Si is reduced in both types of SEI, the irreversible calendar CE still increase (Fig. 4d and Supplementary Figs. 18 and 19). This indicates that Li^+ consumption in n-Si is dominated by SEI dissolution, an effect that will become even more pronounced during extended storage time. TEM and energy-dispersive X-ray spectroscopy (EDS) images of n-Si further visualize the enlarged SEI surface area. Unlike μ-Si, which forms a thin SEI layer outside of large particles, strong C-, O- and F-based SEI signals appear throughout the aggregates of n-Si (Supplementary Fig. 20), indicating a substantially larger SEI-covered surface.

Therefore, although the n-Si reduces active-materials loss (SEI cracking), its large surface area significantly increase SEI growth and accelerate calendar ageing, which might be challenging to resolve solely by electrolyte engineering. This also confirms the limitation of 1 − cCE when comparing systems with different SEI surface areas: the increased cCE of n-Si in $LiPF_6$ EC/DEC/FEC does not align with the actual increase in calendar life, because the SEI dissolution contribute differently. Because the n-Si mitigate SEI cracking, comparing n-Si electrode in different electrolytes (Fig. 4c and Supplementary Fig. 19) could further confirms that LiF is less prone to SEI dissolution compared to organic–inorganic SEI. This also supports that leakage current is a very reliable metric for evaluating calendar life when SEI cracking is largely suppressed.

Overall, SEI dissolution is determined by SEI composition but can be enlarged by higher electrolyte amounts and surface area. Electrolyte amount is typically controlled in industry, so the future strategy should prioritize electrolytes that form inorganic-rich SEI and electrode engineering that minimizes electrolyte–electrodes contact area[56,57], while gradually shifting from nano-size to micro-size materials. As an example of electrode engineering, μ-Si electrodes using a CNT percolating network[58,59] (with reduced carbon content) show reduced calendar ageing (Supplementary Note 6 and Supplementary Fig. 21).

SEI repair/growth due to SEI instability

Both SEI cracking and dissolution weaken passivation and drive continuous SEI repair/growth. Because different SEI components have different thermodynamic stability and electron-blocking ability, their repairing ability varies[60,61]. On the basis of the leakage current results,

https://doi.org/10.1038/s41560-026-01967-1

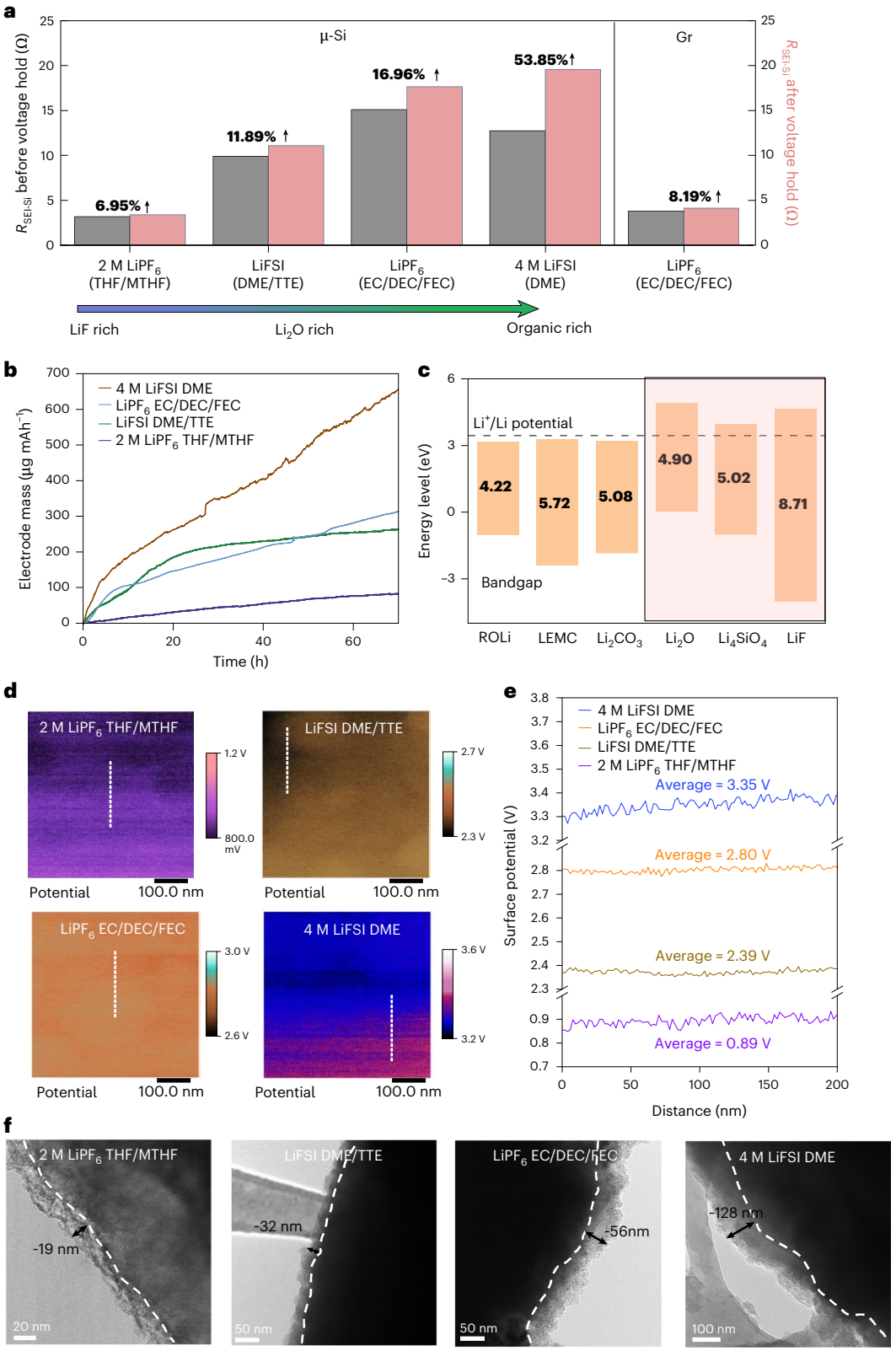

Fig. 5 | SEI growth in different SEI with different repair abilities. a, The comparative bar chart of the resistance increases of $R_{SEI(Si)}$ in a variety of electrolytes in Li | |μ-Si and Li | |graphite cells. **b**, The electrode mass change during the voltage hold tested in situ by the EQCM. **c**, The calculated LUMO energy and bandgap of a variety of SEI compositions. **d**,**e**, The surface potential distribution image and the surface potential of Si anode SEI derived from 2 M $LiPF_6$ THF/MTHF, 1 M LiFSI DME/TTE, 1 M $LiPF_6$ EC/DEC/FEC and 4 M LiFSI DME electrolytes. **f**, The SEI morphology on μ-Si anode after 15 cycles before calendar ageing with 2 M $LiPF_6$ THF/MTHF, 1 M LiFSI DME/TTE, 1 M $LiPF_6$ EC/DEC/FEC and 4 M LiFSI DME electrolytes.

https://doi.org/10.1038/s41560-026-01967-1

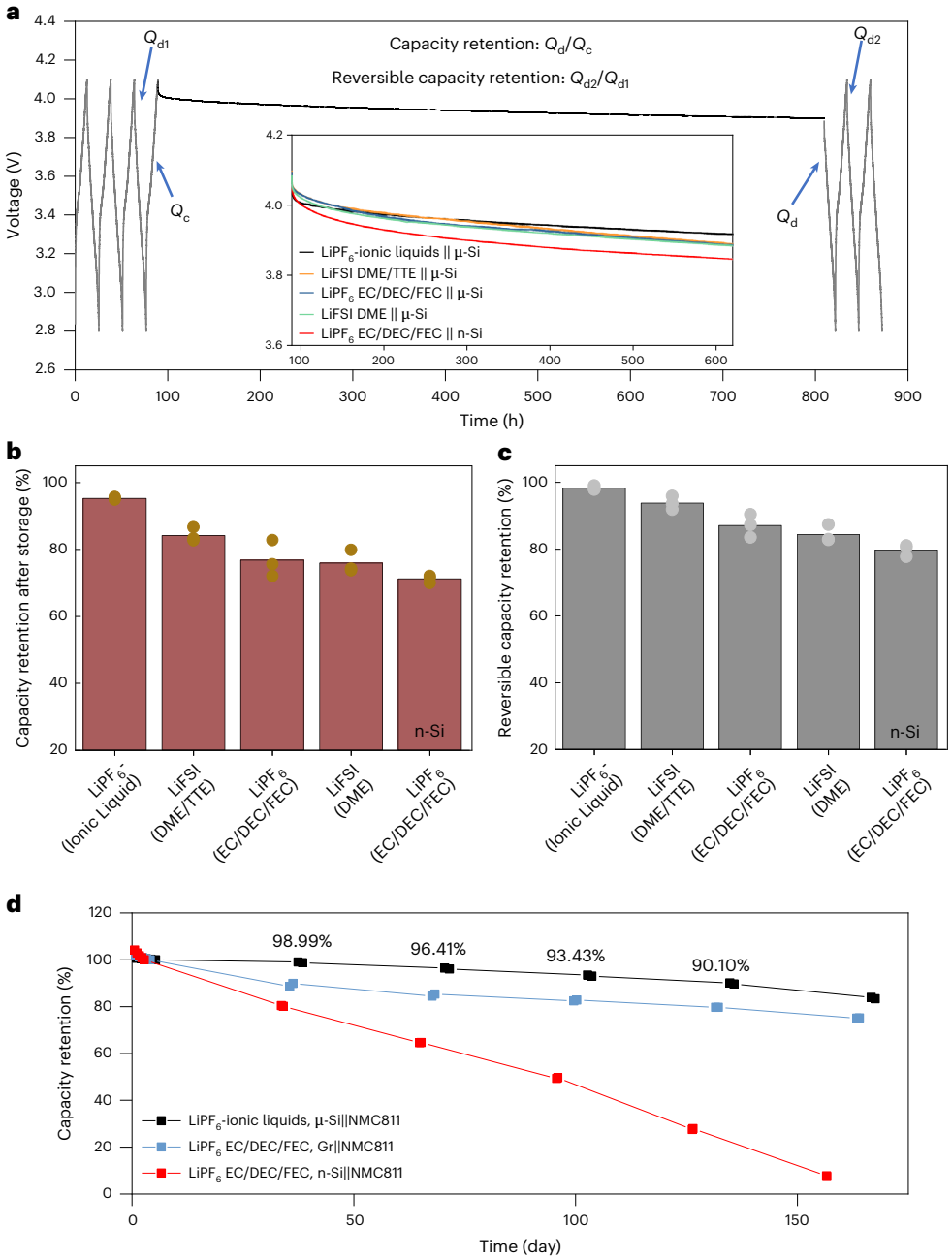

Fig. 6 | Full-cell calendar ageing. a, Open-circuit voltage testing protocol. The inset represents the storage potential profile of μ-Si | |NMC811 cell in $LiPF_6$-ionic liquids, LiFSI DME/TTE, $LiPF_6$ EC/DEC/FEC, LiFSI DME; and of n-Si | |NMC811 cell in $LiPF_6$ EC/DEC/FEC. **b**,**c**, Corresponding capacity retention after storage and reversible capacity retention after storage. Each point represents an independent sample; the bar indicates the mean. **d**, Long-term capacity retention tested with OCV-RPT protocol, which involves real-time open-circuit voltage (OCV) ageing periods with monthly cycles to test capacity loss tests.

the SEI growth in μ-Si anode follows: $LiPF_6$ THF/MTHF < LiFSI DME/TTE < $LiPF_6$ EC/DEC/FEC < LiFSI DME.

Electrochemical impedance spectroscopy (EIS) further (Supplementary Fig. 22) confirmed this trend. Equivalent circuit analysis is provided in Supplementary Note 7 and Supplementary Fig. 23, with the fitted value shown in Supplementary Table 2. Figure 5a summarized the $R_{SEI(Si)}$ increase after voltage hold: LiF-rich SEI in 2 M $LiPF_6$ THF/MTHF exhibits minimal SEI growth (6.95%), indicating a thin and stable SEI. Li_2O-rich SEI increases ~11.89%, organic–inorganic SEI in $LiPF_6$ EC/DEC/FEC increases 16.96%, exceeding that of graphite, confirming that SEI cracking accelerates SEI regrowth, whereas organic-rich SEI exhibited an significant increase of 53.85% in $R_{SEI(Si)}$. The slight increase of LiF-rich SEI, even lower than $R_{SEI(graphite)}$, highlights that SEI-dissolution-driven growth dominates when cracking is limited. The trend is also reflected in the overpotential, with normalized lithiation curves showing progressively larger voltage fade from LiF-rich to organic-rich SEIs (Supplementary Fig. 24a–d).

To quantify SEI repair/growth during calendar ageing, an electrochemical quartz crystal microbalance (EQCM)[33] measure the mass of a sputtered Si thin film on the crystal during calendar ageing (Supplementary Fig. 25). The use of a sputtered Si thin film minimizes the kinetic limitations, thereby enabling a direct investigation on irreversible side reactions[25]. Figure 5b summarizes the mass change of the Si electrode in four sample electrolytes during voltage hold, indicating an increasing tendency from LiF-rich SEI to organic-rich SEI, consistent with trends in calendar ageing and SEI resistance. The higher

https://doi.org/10.1038/s41560-026-01967-1

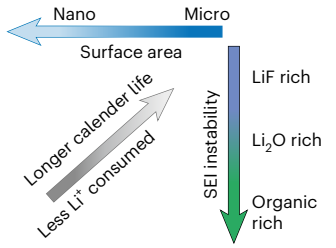

SEI cracking	SEI dissolution	Repair	cCE
Low	Low	High	High
Mediate	Low	Mediate	Mediate
High	High	Low	Low

Fig. 7 | Summary of the relationship between the calendar life and surface area and SEI instability. The calendar life is determined by the SEI surface area and SEI instability. The μ-Si anode has much less surface area than n-Si electrodes. The SEI instability depends on the SEI's ability to suppress crack and dissolution and its passivation ability in the corresponding repair/growth process, which varies in different SEI compositions.

1/dissipation factor suggests a thinner and denser film on the quartz crystal[62], reflecting the inorganic-rich SEI has minimal SEI crack and less SEI growth (Supplementary Fig. 25).

SEI repair ability (passivation ability) is determined by three key properties: thermodynamic stability, electron-blocking ability and solubility. SEI with higher passivation ability require smaller thickness growth (less Li^+ consumption) to repair the SEI. Here we calculated the lowest unoccupied molecular orbital (LUMO) level and bandgap of these SEI components (Fig. 5c). Their potential of valence band maximum and conduction band minimum were obtained using density functional theory surface slab model and aligned to the vacuum potential to assess their reduction ability (Supplementary Fig. 26). LiF exhibits high LUMO energy and the widest bandgap, leading to excellent thermodynamic stability and electron-blocking ability. Li_2O has a narrower bandgap and therefore needs more growth to achieve similar blocking. Furthermore, carbon containing components (ROLi, ROCOLi and Li_2CO_3) are less stable and less electron-blocking, explaining higher Li^+ consumption in these species.

Kelvin probe force microscopy (KPFM) further validates the electron-blocking ability. The lower measured surface potential corresponds to a higher electron work function, which means a higher electron-blocking ability. The KPFM results (Fig. 5d,e) reveal clear differences in surface potential among the SEIs. The relative trend across LiF-rich, Li_2O-rich, inorganic–organic and organic-rich SEIs aligns well with our experimental and calculation results, confirming that LiF-rich SEIs most effectively suppress electron leakage and mitigate calendar ageing through best stability and repairing ability.

TEM and EDS mapping futher visualize SEI repair/growth (Fig. 5f). A clear Si-SEI core shell is observed after calendar ageing in four electrolytes with Si core and a C/O/F outer layer (Supplementary Figs. 27–30), though the SEI thickness varies substantially. As shown in Fig. 5F, the initial SEI thickness increase from 19 nm (2 M $LiPF_6$ THF/MTHF) to 32 nm (1 M LiFSI DME/TTE), 56 nm (1 M $LiPF_6$ EC/DEC/FEC) and 128 nm (4 M LiFSI DME). Thinner SEIs exhibit denser structures, whereas less dense and less protective SEIs require greater thickness to achieve stabilization. This trend follows the compositional hierarchy: LiF-rich SEI offers the strongest passivation and lowest dissolution, resulting in the lowest thickness.

We further examined the SEI thickness after calendar ageing (Supplementary Fig. 31). The SEI increased to 22 nm, 41 nm, 79 nm and 210 nm after calendar ageing. Whereas TEM alone cannot quantify SEI growth, the systematic thickening correlates strongly with increasing organic content and decreasing inorganic content, in agreement with observed SEI growth and SEI repair ability in different electrolytes. Depth profiling of XPS Si spectra further validates this trend, as reflected by the varying intensity of $LiSi_x$ signals across different SEIs (Supplementary Note 8 and Supplementary Fig. 32).

Full-cell performance with ageing

The voltage-hold protocol facilitates screening, but it remains essential to quantify actual calendar ageing in μ-Si | |NMC811 full cells. Figure 6 presents OCV evolution for representative electrolytes, including $LiPF_6$-ionic liquids (LiF-rich SEI), LiFSI DME/TTE (Li_2O-rich SEI), $LiPF_6$ EC/DEC/FEC (organic–inorganic SEI) and LiFSI DME (organic-rich SEI). $LiPF_6$ THF/MTHF was replaced with $LiPF_6$-ionic liquids due to the poor anodic stability[31], which does not support NMC811 cathode. The $LiPF_6$-ionic liquids is based on pyrrolidinium cation and PF_6^- anion, promoting preferential PF_6^- reduction to form robust LiF SEI[38], while also exhibiting high anodic stability compatible with NMC811 cathode, enabling excellent cycling performance (Supplementary Fig. 33).

The conclusions from Si | |NMC811 OCV storage (Fig. 6a–c) and Li | |Si voltage hold are fully consistent across different electrolytes and electrodes: those that form LiF-rich SEIs outperform those that form Li_2O-rich and organic-rich SEIs. μ-Si | |NMC811 with $LiPF_6$-ionic liquids exhibit the highest capacity retention of 95.3% (Fig. 6b) and reversible capacity retention of 98.3% (Fig. 6c) after 1 month storage, reflecting minimal SEI instability and SEI repair/growth. The reversible capacity retention (Fig. 6c) also correlates with the low-rate cCE in full cells (Supplementary Fig. 33), highlighting cCE as a relative predictive indicator for calendar life in systems with similar particle sizes. Finally, μ-Si | |NMC811 consistently shows a slower voltage fading and higher capacity retention than n-Si | |NMC811 due to reduced SEI dissolution.

We also performed long-term calendar ageing measurements using the USABC protocol[30] (protocol in Supplementary Fig. 34), which applies monthly reference performance tests (RPTs) during storage. Capacity fading is shown in Fig. 6d with cycling profiles shown in Supplementary Fig. 35. The μ-Si | |NMC811 cell with $LiPF_6$-ionic liquids showed excellent stability, retaining 98.99% capacity after one month and 90.1% after four months, comparable to $LiPF_6$ EC/DEC/FEC in Gr | |NMC811 cell. By sharp contrast, although n-Si mitigates SEI cracking and cycles stably in n-Si | |NMC811 cell with $LiPF_6$ EC/DEC/FEC (Supplementary Fig. 33e), its large surface area cause severe calendar fading (~20% loss per month).

Overall, both cycle and calendar ageing are derived from SEI instability (cracking and dissolution). Calendar life is typically more sensitive to SEI dissolution compared to cycle life, whereas the role of SEI cracking depends on electrode volume change and SEI properties. For μ-Si, significant volume expansion makes SEI cracking non-negligible in calendar ageing. Our results show that electrolytes significantly affect SEI instability and repair ability, as summarized in Fig. 7. LiF-rich SEI suppresses SEI cracking, has low solubility and electronic conductivity with high thermodynamic stability, minimizing SEI repair/growth and improving calendar life. Organic-rich SEI is less stable, more soluble and conductive, requiring more Li^+ for repair, leading to faster ageing. Thus, calendar life consistently decreases from LiF-rich to organic-rich SEIs.

Cycle life follows the same trend on these properties, cCE across electrolytes align consistently with the observed trend from LiF-rich to organic-rich SEI[36,63] (Fig. 7). Because both calendar life and cycle life are intrinsically linked to SEI cracking and dissolution, cCE could serve as a valuable predictive indicator when SEI dissolution is not dominated. This indicator, together with the traditional leakage current, enables more accurate and reliable early-stage calendar ageing screening.

Therefore, this study investigates calendar ageing across various electrolytes with Si anodes of different sizes. Whereas SEI dissolution is often thought to be more pronounced in calendar life, its dependence on particle size and the role of SEI cracking warrant serious consideration. We observe a diminishing trend in SEI stability and repairability from LiF-rich to organic-rich SEI, leading to progressively increase calendar ageing in the same electrodes. We further demonstrate that cCE could serve as a valuable complementary metric in early-stage calendar life evaluation. Particle size remains critical: n-Si with high surface area suffers amplifies SEI dissolution, thus requiring strategy to reduce electrolyte–electrode contact area for better calendar life.

For example, dispersing n-Si in a dense carbon matrix or other suitable matrix[57] to minimize the contact area can enhance calendar life. These insights highlight the need for future research to jointly optimize electrolyte/SEI chemistry and electrode architecture. Given the intrinsically linked mechanism governing both cycle and calendar life, advancing both simultaneously is both necessary and feasible. This work provides a comprehensive understanding connecting cCE, SEI compositions, Si particle size and calendar life, offering insights in the screening of electrolyte and electrode designs towards extended calendar life.

Methods

Materials and preparation of electrolytes

THF (Tetrahydrofuran, anhydrous, ≥99.9%, inhibitor-free), MTHF (BioRenewable, anhydrous, ≥99%, inhibitor-free) and DME(1,2-dimethoxyethane, 99.9%, inhibitor-free) were from Sigma-Aldrich. TTE (1,1,2,2-tetrafluoroethyl-2,2,3,3-tetrafluoropropyl ether, >95%) was from TCI America. $LiPF_6$ and FEC was from Gotion. These solvents were dried by molecular sieves overnight. To prepare solvents: 1 M $LiPF_6$ EC/DEC (lithium hexafluorophosphate in ethylene carbonate and diethyl carbonate, 1.0 M $LiPF_6$ in EC/DEC = 50/50 (v/v), battery grade); 1 M $LiPF_6$ EC/DEC/FEC was prepared by adding 10 wt% FEC in 1 M $LiPF_6$ EC/DEC and then adding $LiPF_6$ to make it a 1 M $LiPF_6$ solution; 2M $LiPF_6$ THF/MTHF was prepared by a 1:1 v/v mixture of THF and MTHF; 1 M LiFSI DME/TTE was prepared with a molar ratio of LFSI: DME: TTE = 1:1.2:3. The $LiPF_6$-ionic liquid electrolytes were synthesized and prepared as reported[38].

The Si electrodes were prepared as described previously[31]: the slurry was first prepared by dispersing silicon microparticles (325 mesh, as received), lithium polyacrylate binder (10 wt% aqueous solution) and Ketjen black 300 in water with a weight ratio of 6:2:2. The slurry was cast on a copper foil and dried at room temperature overnight and further dried at 90 °C under vacuum. CR2032 coin-type half cells were assembled by sandwiching one piece of polyethylene separator (Celgard) and one piece of glass fibre between the silicon electrodes and Li metal foil. The high electrolyte amount cell used two more glass fibre to accommodate the electrolytes.

Electrode materials and composition

Active materials: silicon microparticles (325 mesh, Sigma-Aldrich)

Binder: lithium polyacrylate (prepared by neutralizing poly(acrylic acid), Mw ~250,000, Sigma-Aldrich).

Conductive agent: Ketjen Black EC-300J (Fuel Cell Store).

Composition ratio: 6:2:2 by weight (Si:Carbon:Binder)

Coin cell configuration and electrochemical set-up

All tests were conducted using CR2032 coin cells assembled in an argon-filled glovebox (O_2 and H_2O < 0.1 ppm).

Half-cell configuration: Li metal was used as the counter/reference electrode. The Si anode had an areal capacity of 3.5–4 mAh cm^{-2}. A stack of one PE separator and one GF/F glass fibre separator (Whatman, ~260μm thick) was used. Electrolyte volume was 150 μl. One 1-mm spacer is used. The high electrolyte amount cell used two more glass fibres to accommodate the electrolytes.

Full-cell configuration: NMC811 was used as the cathode (~3 mAh cm^{-2}) paired with a Si anode (~4.2 mAh cm^{-2}). A single PE separator was used, with an electrolyte volume of 30 μl. Two 1-mm spacers are used.

Assembly procedure

Coin cells (CR2032 type) were assembled in an argon-filled glovebox (H_2O < 0.1 ppm, O_2 < 0.1 ppm). The typical stacking procedure was as follows:

Anode placement: the silicon working electrode (or graphite) was first placed at the bottom of the coin cell casing.

Separator and electrolyte addition: a polyethylene (PE) separator was placed on top of the anode, followed by dropwise addition of electrolyte to allow full wetting and absorption. For half-cell configurations, a glass fibre (GF/F) separator was additionally stacked to enhance electrolyte retention.

Counter electrode and spacers: a lithium metal disc (or NMC cathode for full cells) was placed as the counter electrode. Stainless-steel spacers and a spring were inserted on top.

Crimping: the cell was sealed using a crimping machine, ensuring tight compression and uniform contact.

The assembled cells were rested for 8–12 hours before initiating electrochemical testing to allow for complete electrolyte wetting.

Testing protocol

The calendar life was tested on Arbin Test Equipment with an accuracy of ± 2 mV and ± 10 nA. The typical calendar life test starts with 15 formation cycles in the voltage window of 0.06–1 V for Si | |Li cell followed by a 180 h hold at 0.06 V. There are three diagnostic cycles before the voltage hold and two diagnostic cycles after the voltage hold at C/15 rate. Meantime, to reduce the influence of the concentration gradient, the delithiation before voltage hold and after voltage hold need to be fully delithiation by constant voltage charge until reaching a current of C/100. Note: for electrolytes whose SEI is susceptible to oxidation around 1 V, this step should be skipped if significant capacity is observed during this process. Electrochemical impedance spectroscopy (EIS) tests in the frequency range from 100 kHz to 0.001 Hz were carried out using a Gamry workstation at full delithiation state. The resistance testing was built into the Arbin tester to have in situ testing. The analysis of EIS spectra was done on Z-View.

Characterizations

X-ray photoelectron spectroscopy (XPS) measurements were acquired with a K-alpha Thermo system using Al Kα radiation (hν = 1,486.6 eV) under ultra-high vacuum (< 1×10^{-12} atm) with a measured spot size of 400 μm in diameter. A flood gun was used during the analysis to compensate for the charging of the samples The Si electrodes for XPS analysis were carefully extracted from coin cells in an argon-filled glovebox. After disassembly, the electrodes were gently rinsed with corresponding pure solvent (THF/MTHF, DME, EC/DEC/FEC and DME), depending on the electrolyte system, to remove residual salts without disturbing the SEI. The rinsed samples were then dried under vacuum at room temperature inside the glovebox antechamber. All samples were transferred to the XPS instrument using an air-tight, vacuum-sealed transfer vessel to prevent air exposure. Sputter depth profiling was carried out using an Ar+ ion gun with ion energy at 200 eV with a roster size of 2 mm. The angle between the surface normal and the ion gun beam was 0°. The binding energy was corrected based on the C 1*s* spectrum, assigning C–C to 284.8 eV. Relative atomic concentrations were calculated by integrating respective peaks with a Shirley background, using The CasaXPS software, accounting for respective atomic sensitivity factors. The composition and thickness of the SEI were also explored via scanning transmission electron microscopy (STEM)–EDX mapping with a Hitachi HD2700C dedicated STEM with a probe corrector operated at 200 kV.

EQCM measurements were performed using an EQCM 10 M Quartz Crystal Microbalance from Gamry Instruments. We sputtered a 100-nm Si layer onto the quartz crystal using the AJA ATC 1800 Sputtering unit. This Si-coated quartz crystal served as the working electrode. For the counter and reference electrode, we used Li metal. The EQCM cell was assembled in a glovebox filled with argon, maintaining an O_2/H_2O concentration of <0.1 ppm. We connected the EQCM to battery test system for electrochemical tests conducted at 25 °C. The mass change was calculated using the Sauerbrey equation (equation (4)).

$$\Delta f = -\frac{2{f_0}^2}{A\sqrt{\mu_q \rho_q}}\Delta m \tag{4}$$

Here f_0 represents the fundamental frequency of the crystal, A is the piezoelectrically active crystal area and μ_q and ρ_q are the shear modulus and density of the quartz, respectively. The mass change (Δm) can be determined based on the frequency change (Δf). The dissipation factor (ΔD) was calculated by equation (5).

$$\Delta D = \frac{\Delta f_{FWHM}}{f_c} \quad (5)$$

where f_c represents the centre frequency and Δf_{FWHM} denotes the full-width at half-maximum.

PeakForce Kelvin probe force microscopy (PF-KPFM) was used to measure the work function of SEI layers formed with different electrolytes. The measurements were carried out using a Bruker Dimension Icon scanning probe microscope system inside an Ar-filled glovebox, where H_2O and O_2 levels were maintained below 0.1 ppm. The AM-KPFM mode was used with a conductive SCM-PIT-V2 probe. Before measuring the SEI layers, the probe work function was calibrated by recording the contact potential difference on a freshly cleaved highly oriented pyrolytic graphite substrate. The scan area was set to 500 nm × 500 nm with a scan rate of 1 Hz. Because the work function of a clean highly oriented pyrolytic graphite surface is known to be 4.6 eV (ref. 64), the tip work function ($\varnothing_{tip}$) was determined using the equation (6).

$$\varnothing_{sample} = \varnothing_{tip} - V_{\frac{sample}{tip}} e \quad (6)$$

where $\varnothing_{sample}$ and $\varnothing_{tip}$ are the work functions of the sample and the tip, respectively; $V_{sample\text{-}tip}$ is the measured surface potential between the sample surface and the tip; and e is the elementary charge. This yielded a value of 4.78 eV. Using this calibrated probe, the work function of a freshly cleaned Au substrate was measured to be 5.44 eV, in excellent agreement with reported values[65], thereby confirming the reliability of this measurement approach.

Computational details

Density functional theory calculations were carried out using the Vienna ab initio simulation package (VASP) 6.3 code[66]. The projector augmented wave (PAW) potentials were adopted and Perdew–Burke–Ernzerhof (PBE) realization of the generalized gradient approximation (GGA) for the exchange correlation was performed[67,68]. The kinetic energy cut-offs of 520 were used for all calculations. The Brillouin zone was sampled with Monkhorst–Pack k-point grid[69]. The surfaces slabs were constructed by cleaving the optimized bulk structures along low-index facets with lowest energy surface. A vacuum layer of at least 15 Å was added. All atoms were relaxed fully until the force on them was less than 0.03 eV $Å^{-1}$ and then performed self-consistent field calculation. The plane-averaged electrostatic potential and macroscopic-averaged electrostatic potential were extracted using VASPKIT. The potential of conduction band minimum and valence band maximum was aligned with respect to the vacuum potential of 4 eV.

Data availability

The authors declare that all data supporting the findings of this study are available within the paper and Supplementary Information files. Source data are provided with this paper.

References

1. Lin, D., Liu, Y. & Cui, Y. Reviving the lithium metal anode for high-energy batteries. *Nat. Nanotechnol.* **12**, 194–206 (2017).
2. Cheng, X.-B., Zhang, R., Zhao, C.-Z. & Zhang, Q. Toward safe lithium metal anode in rechargeable batteries: a review. *Chem. Rev.* **117**, 10403–10473 (2017).
3. Duffner, F. et al. Post-lithium-ion battery cell production and its compatibility with lithium-ion cell production infrastructure. *Nat. Energy* **6**, 123–134 (2021).
4. Heubner, C. et al. From lithium-metal toward anode-free solid-state batteries: current developments, issues, and challenges. *Adv. Funct. Mater.* **31**, 2106608 (2021).
5. Ge, M. et al. Recent advances in silicon-based electrodes: from fundamental research toward practical applications. *Adv. Mater.* **33**, 2004577 (2021).
6. Li, H. et al. Revisiting the preparation progress of nano-structured si anodes toward industrial application from the perspective of cost and scalability. *Adv. Energy Mater.* **12**, 2102181 (2022).
7. Peled, E. & Menkin, S. SEI: past, present and future. *J. Electrochem. Soc.* **164**, A1703 (2017).
8. Sina, M. et al. Direct visualization of the solid electrolyte interphase and its effects on silicon electrochemical performance. *Adv. Mater. Interfaces* **3**, 1600438 (2016).
9. Michan, A. L. et al. Solid electrolyte interphase growth and capacity loss in silicon electrodes. *J. Am. Chem. Soc.* **138**, 7918–7931 (2016).
10. Cui, L.-F., Yang, Y., Hsu, C.-M. & Cui, Y. Carbon–silicon core– shell nanowires as high capacity electrode for lithium ion batteries. *Nano Lett.* **9**, 3370–3374 (2009).
11. Cui, L.-F., Ruffo, R., Chan, C. K., Peng, H. & Cui, Y. Crystalline-amorphous core–shell silicon nanowires for high capacity and high current battery electrodes. *Nano Lett.* **9**, 491–495 (2009).
12. Chen, H. et al. Milled flake graphite/plasma nano-silicon@ carbon composite with void sandwich structure for high performance as lithium ion battery anode at high temperature. *Carbon* **130**, 433–440 (2018).
13. Yao, Y. et al. Interconnected silicon hollow nanospheres for lithium-ion battery anodes with long cycle life. *Nano Lett.* **11**, 2949–2954 (2011).
14. Ge, M. et al. Large-scale fabrication, 3D tomography, and lithium-ion battery application of porous silicon. *Nano Lett.* **14**, 261–268 (2014).
15. Kim, H., Seo, M., Park, M. & Cho, J. A critical size of silicon nano-anodes for lithium rechargeable batteries. *Angew. Chem. Int. Ed.* **49**, 2146–2149 (2010).
16. McBrayer, J. D. et al. Calendar aging of silicon-containing batteries. *Nat. Energy* **6**, 866–872 (2021).
17. Kim, N., Kim, Y., Sung, J. & Cho, J. Issues impeding the commercialization of laboratory innovations for energy-dense Si-containing lithium-ion batteries. *Nat. Energy* **8**, 921–933 (2023).
18. Jia, H. et al. High-performance silicon anodes enabled by nonflammable localized high-concentration electrolytes. *Adv. Energy Mater.* **9**, 1900784 (2019).
19. Cao, Z., Zheng, X., Qu, Q., Huang, Y. & Zheng, H. Electrolyte design enabling a high-safety and high-performance Si anode with a tailored electrode–electrolyte interphase. *Adv. Mater.* **33**, 2103178 (2021).
20. Jeong, M.-G. et al. Self-rearrangement of silicon nanoparticles embedded in micro-carbon sphere framework for high-energy and long-life lithium-ion batteries. *Nano Lett.* **17**, 5600–5606 (2017).
21. Veith, G. M. et al. Determination of the solid electrolyte interphase structure grown on a silicon electrode using a fluoroethylene carbonate additive. *Sci. Rep.* **7**, 6326 (2017).
22. Lam, S. et al. Surprising relationship between silicon anode calendar aging and electrolyte components in a localized high concentration electrolyte system. *ACS Appl. Mater. Interfaces* **17**, 43020–43033 (2025).
23. Ha, Y. et al. Effect of water concentration in LiPF6-based electrolytes on the formation, evolution, and properties of the solid electrolyte interphase on Si anodes. *ACS Appl. Mater. Interfaces* **12**, 49563–49573 (2020).
24. Veith, G. M. et al. Direct determination of solid-electrolyte interphase thickness and composition as a function of state of charge on a silicon anode. *J. Phys. Chem. C* **119**, 20339–20349 (2015).

25. McBrayer, J. D. et al. Scanning electrochemical microscopy reveals that model silicon anodes demonstrate global solid electrolyte interphase passivation degradation during calendar aging. *ACS Appl. Mater. Interfaces* **16**, 19663–19671 (2024).
26. Kalaga, K., Rodrigues, M.-T. F., Trask, S. E., Shkrob, I. A. & Abraham, D. P. Calendar-life versus cycle-life aging of lithium-ion cells with silicon-graphite composite electrodes. *Electrochim. Acta* **280**, 221–228 (2018).
27. Zhang, Y. et al. Silicon anodes with improved calendar life enabled by multivalent additives. *Adv. Energy Mater.* **11**, 2101820 (2021).
28. Verma, A. et al. Significant improvements to Si calendar lifetime using rapid electrolyte screening via potentiostatic holds. *J. Electrochem. Soc.* **171**, 070539 (2024).
29. Schulze, M. C. et al. Critical evaluation of potentiostatic holds as accelerated predictors of capacity fade during calendar aging. *J. Electrochem. Soc.* **169**, 050531 (2022).
30. McBrayer, J. D., Harrison, K. L., Allcorn, E. & Minteer, S. D. Chemical contributions to silicon anode calendar aging are dominant over mechanical contributions. *Front. Batteries Electrochem.* **2**, 1308127 (2023).
31. Chen, J. et al. Electrolyte design for LiF-rich solid–electrolyte interfaces to enable high-performance microsized alloy anodes for batteries. *Nat. Energy* **5**, 386–397 (2020).
32. Hasa, I. et al. Electrochemical reactivity and passivation of silicon thin-film electrodes in organic carbonate electrolytes. *ACS Appl. Mater. Interfaces* **12**, 40879–40890 (2020).
33. Sayavong, P. et al. Dissolution of the solid electrolyte interphase and its effects on lithium metal anode cyclability. *J. Am. Chem. Soc.* **145**, 12342–12350 (2023).
34. Zhang, W. et al. Recovery of isolated lithium through discharged state calendar ageing. *Nature* **626**, 306–312 (2024).
35. Stetson, C. et al. Temperature-dependent solubility of solid electrolyte interphase on silicon electrodes. *ACS Energy Lett.* **4**, 2770–2775 (2019).
36. Boyle, D. T. et al. Corrosion of lithium metal anodes during calendar ageing and its microscopic origins. *Nat. Energy* **6**, 487–494 (2021).
37. Harlow, J. E. et al. A wide range of testing results on an excellent lithium-ion cell chemistry to be used as benchmarks for new battery technologies. *J. Electrochem. Soc.* **166**, A3031 (2019).
38. Li, A.-M. et al. Asymmetric electrolyte design for high-energy lithium-ion batteries with micro-sized alloying anodes. *Nat. Energy* **9**, 1551–1560 (2024).
39. Wang, A., Kadam, S., Li, H., Shi, S. & Qi, Y. Review on modeling of the anode solid electrolyte interphase (SEI) for lithium-ion batteries. *npj Comput. Mater.* **4**, 15 (2018).
40. Tan, J., Matz, J., Dong, P., Shen, J. & Ye, M. A growing appreciation for the role of LiF in the solid electrolyte interphase. *Adv. Energy Mater.* **11**, 2100046 (2021).
41. Käbitz, S. et al. Cycle and calendar life study of a graphite| $LiNi_{1/3}Mn_{1/3}Co_{1/3}O_2$ Li-ion high energy system. Part A: full cell characterization. *J. Power Sources* **239**, 572–583 (2013).
42. Gauthier, R. et al. How do depth of discharge, C-rate and calendar age affect capacity retention, impedance growth, the electrodes, and the electrolyte in Li-ion cells?. *J. Electrochem. Soc.* **169**, 020518 (2022).
43. Naumann, M., Schimpe, M., Keil, P., Hesse, H. C. & Jossen, A. Analysis and modeling of calendar aging of a commercial $LiFePO_4$/graphite cell. *J. Energy Storage* **17**, 153–169 (2018).
44. Keil, P. et al. Calendar aging of lithium-ion batteries. *J. Electrochem Soc.* **163**, A1872 (2016).
45. Qian, J. et al. High rate and stable cycling of lithium metal anode. *Nat. Commun.* **6**, 6362 (2015).
46. Chen, J. et al. Electrolyte design for Li metal-free Li batteries. *Mater. Today* **39**, 118–126 (2020).
47. Cao, X. et al. Monolithic solid–electrolyte interphases formed in fluorinated orthoformate-based electrolytes minimize Li depletion and pulverization. *Nat. Energy* **4**, 796–805 (2019).
48. Johnson, N. M. et al. Enabling silicon anodes with novel isosorbide-based electrolytes. *ACS Energy Lett.* **7**, 897–905 (2022).
49. Verma, A. et al. Assessing electrolyte fluorination impact on calendar aging of blended silicon-graphite lithium-ion cells using potentiostatic holds. *J. Electrochem. Soc.* (2023).
50. Kim, M. et al. A new mechanism of stabilizing SEI of Si anode driven by crosstalk behavior and its potential for developing high performance Si-based batteries. *Energy Storage Mater.* **55**, 436–444 (2023).
51. Tan, S. et al. Synchronized breathing in anion-derived interphases. *ACS Energy Lett.* **10**, 3746–3754 (2025).
52. Langdon, J. & Manthiram, A. Crossover effects in batteries with high-nickel cathodes and lithium-metal anodes. *Adv. Funct. Mater.* **31**, 2010267 (2021).
53. Jeong, H. & Johnson, C. S. Reactivity of carbonate solvent electrolytes on lithium silicon anodes. *ACS Appl. Mater. Interfaces* **17**, 54633–54645 (2025).
54. Huo, H. et al. Chemo-mechanical failure mechanisms of the silicon anode in solid-state batteries. *Nat. Mater.* **23**, 543–551 (2024).
55. Lu, W., Zhang, L., Qin, Y. & Jansen, A. Calendar and cycle life of lithium-ion batteries containing silicon monoxide anode. *J. Electrochem. Soc.* **165**, A2179 (2018).
56. Sung, J. et al. Subnano-sized silicon anode via crystal growth inhibition mechanism and its application in a prototype battery pack. *Nat. Energy* **6**, 1164–1175 (2021).
57. Adhikari, P. R. et al. The origin of improved performance in boron-alloyed silicon nanoparticle-based anodes for lithium-ion batteries. *Adv. Energy Mater.* 2501074 (2025).
58. Lee, T. et al. Fast-chargeable lithium-ion batteries by μ-Si anode-tailored full-cell design. *Proc. Natl Acad. Sci. USA* **122**, e2417053121 (2025).
59. Park, S.-H. et al. High areal capacity battery electrodes enabled by segregated nanotube networks. *Nat. Energy* **4**, 560–567 (2019).
60. Horstmann, B., Single, F. & Latz, A. Review on multi-scale models of solid-electrolyte interphase formation. *Curr. Opin. Electrochem.* **13**, 61–69 (2019).
61. Wang, E. et al. Mitigating electron leakage of solid electrolyte interface for stable sodium-ion batteries. *Angew. Chem. Int. Ed.* **62**, e202216354 (2023).
62. Yang, Z., Dixon, M. C., Erck, R. A. & Trahey, L. Quantification of the mass and viscoelasticity of interfacial films on tin anodes using EQCM-D. *ACS Appl. Mater. Interfaces* **7**, 26585–26594 (2015).
63. Yu, Z. et al. Molecular design for electrolyte solvents enabling energy-dense and long-cycling lithium metal batteries. *Nat. Energy* **5**, 526–533 (2020).
64. Bai, R., Tolman, N. L., Peng, Z. & Liu, H. Influence of atmospheric contaminants on the work function of graphite. *Langmuir* **39**, 12159–12165 (2023).
65. Sachtler, W. M. H., Dorgelo, G. J. H. & Holscher, A. A. The work function of gold. *Surf. Sci.* **5**, 221–229 (1966).
66. Kresse, G. & Furthmüller, J. Efficient iterative schemes for ab initio total-energy calculations using a plane-wave basis set. *Phys. Rev. B* **54**, 11169 (1996).
67. Perdew, J. P., Burke, K. & Ernzerhof, M. Generalized gradient approximation made simple. *Phys. Rev. Lett.* **77**, 3865 (1996).
68. Kohn, W. & Sham, L. J. Self-consistent equations including exchange and correlation effects. *Phys. Rev.* **140**, A1133 (1965).
69. Hendrik, J. M. & James, D. P. Special points for Brillouin-zone integrations. *Phys. Rev. B* **13**, 5188–5192 (1976).

Acknowledgements
This research was supported by US Department of Energy, Vehicle Technologies Office (DOE-VTO) under the Silicon Consortium Project, directed by N. Eidson, C. Steinway, T. Do and B. Cunningham, and managed by A. Burrell. The was supported by DOE Office of Energy Efficiency and Renewable Energy (EERE) grant DE-EE0009183 (W.Z. and C.W.) We acknowledge the technical support from the Maryland NanoCenter.

Author contributions
W.Z. conceived the idea, performed experiments and wrote the manuscript. N.Z. performed EQCM measurements and assisted with electrochemical tests. Z.W. performed calculations. A.-M.L. provided ionic liquids and assisted with related full-cell ageing. S.L., Y.L. and Z.L. helped with the testing. T.L., Y.C. and L.Z. helped on electrode engineering. H.W., S.-C.L. and J. Rao helped on transmission electron microscopy. J. Roschella edited and improved the manuscript. Z.Z. and H.H. conduced the AFM at Rutgers University. B.L.L. helped with the XPS test. C.S.J. guided the analysis and manuscript writing. C.W. supervised the study and the manuscript writing. All authors discussed the results.

Competing interests
The authors declare no competing interests.

Additional information
Supplementary information The online version contains supplementary material available at https://doi.org/10.1038/s41560-026-01967-1.

Correspondence and requests for materials should be addressed to Chunsheng Wang.

Peer review information *Nature Energy* thanks Josefine McBrayer and the other, anonymous, reviewer(s) for their contribution to the peer review of this work.

Reprints and permissions information is available at www.nature.com/reprints.

Publisher's note Springer Nature remains neutral with regard to jurisdictional claims in published maps and institutional affiliations.

Springer Nature or its licensor (e.g. a society or other partner) holds exclusive rights to this article under a publishing agreement with the author(s) or other rightsholder(s); author self-archiving of the accepted manuscript version of this article is solely governed by the terms of such publishing agreement and applicable law.

© The Author(s), under exclusive licence to Springer Nature Limited 2026